Title Page

Title

The Virtual Nose: Assessment of Static Nasal Airway Obstruction Using Computational Simulations and 3D Printed Models

List of Authors

Insert full names of all authors, academic degrees, titles (positions)

1. [a]Alex W N Reid, FRCS(Plast) BM BChir MA(Cantab) Dip Hand Surg (Br) FEBHS, Locum Consultant Plastic Surgeon
2. [b]Xinye Chen, MEng
3. [b]Haoxiang Wen, MEng
4. [b]Haoyuan Li, MEng
5. [b]Zhixing Wang, MEng
6. [b]Yanchang Hu, MEng
7. [b]Feng'Ao Zhang, MEng
8. [b]Eral Bele, PhD, CEng, Lecturer (Teaching)
9. [b]PJ Tan, PhD, MSc, BEng, Associate Professor of Applied Mechanics
10. [c]Charles East, FRCS, MBBS, Consultant Otolaryngologist and Facial Plastic Surgeon

Institutional Affiliations

a. Addenbrooke's Hospital, Cambridge CB2 0QQ, UK
b. Department of Mechanical Engineering, University College London, Torrington Place, London WC1E 7JE, UK
c. Department of ENT/Facial Plastic Surgery, University College Hospitals London NHS Trust, London NW1 2BU, UK

Corresponding Author

Alex W N Reid, FRCS(Plast) BM BChir MA(Cantab) Dip Hand Surg (Br) FEBHS, Locum Consultant Plastic Surgeon
Addenbrooke's Hospital, Cambridge CB2 0QQ, UK
E-mail: awnr2@cantab.net

Authorship Statement

All authors have made substantial contributions to the design, analysis, interpretation, writing or revising the work for content, final approval of the final version to be published and are agree to be accountable for all aspects of the work in ensuring that questions related to the accuracy or integrity of any part of the work are appropriately investigated and resolved.

Disclosures

The authors declared no potential conflicts of interest with respect to the research, authorship, and publication of this article

Funding

The authors received a £4000 grant from the Department of Mechanical Engineering, University College London to fund the purchase of test equipment and the 3D printing of nasal models

Novelty Statement

- Experimental measurements of airflow in 3D printed nasal channels performed for first time
- Airflow pressure and velocity fields were characterised through experimental measurements and computational simulations for healthy and collapsed nasal channels
- Proposal of incremental nasal resistance as a measure to assess NAO
- Analysis of the flow field indicated that the NAO in the nasal valve

increases significantly the wall pressure, shear stress, and incremental resistance behind the obstruction; requiring further investigations

Acknowledgement Toms Ivars and Dr Veronique Sauret-Jackson of Cavendish Imaging, 109 Harley Street, London W1G 6AN; A/Prof Ryo Torii of UCL Mechanical Engineering for helpful discussions and access to Simpleware.

Key Points

Question

Can virtual simulations of nasal airflow in patients seeking septorhinoplasty be validated by experimental data? Can they potentially be employed as diagnostic tools for objective assessment of nasal airflow?

Findings

Computer flow dynamic models correlated with experimental measurements using a novel method of 3D printed models of noses based on patient cone beam CT scans.

Within the nasal valve, the parameters of wall pressure, shear stress and incremental resistance increase significantly behind a nasal airway obstruction.

Meaning

Both 3D printed and virtual noses are potentially useful tools for pre- and post-operative assessment of septorhinoplasty.

Abstract

Background

The use of virtual noses to predict the outcome of surgery is of increasing interests; particularly, as detailed and objective pre- and post-operative assessments of nasal airway obstruction are difficult to perform. The objective of this paper is to validate predictions using virtual noses against their experimentally measured counterpart in rigid 3D printed models.

Methods

Virtual nose models, with and without nasal airway obstruction, were reconstructed from patients' cone beam computed tomography scans; and, used to evaluate airflow characteristics through computational fluid dynamics simulations. Prototypes of the reconstructed models were 3D-printed and instrumented experimentally for pressure measurements.

Results

Correlation between the numerical predictions and experimental measurements was shown. Analysis of the flow field indicated that the nasal airway obstruction in the nasal valve increases significantly the wall pressure, shear stress, and incremental nasal resistance behind the obstruction.

Conclusions

Airflow predictions in static virtual noses correlate well with detailed experimental measurements on 3D printed replicas of patient airways.

Background

Patients who have had septorhinoplasty for nasal airway obstruction (NAO) are frequently dissatisfied with the outcome because in many cases the NAO symptoms persist, with studies indicating up to 50% of patients reported recurring NAO symptoms post septoplasty.[1,2]

NAO is a highly subjective symptom[3] and has a variety of causes including congestion (allergic and non-allergic rhinitis) or problematic anatomy (such as a deviated nasal septum, turbinate hypertrophy or nasal valve compromise). The nasal valve (or 'nasal gateway'[4]) is the flow limiting-region of the nose[2] beginning approximately 2 cm from the nostrils and to at least 1 cm beyond the pyriform. Pre-operative planning for NAO surgery is typically based on the patient symptoms, clinical findings and imaging, rather than a detailed objective assessment/measurement of airflow, which is difficult to perform[5] owing to the complex morphology and inaccessibility of the nasal channels.[6,7] Functional measurements from rhinomanometry and acoustic rhinometry provide measures of average pressure and flow during inspiration and expiration but these are overall measurements: they do not fully appraise NAO in detail and do not necessarily correspond to the symptoms of individual patient.[8]

In recent years there has been interest in virtual simulation of the airflow in the nasal channels using Computational Fluid Dynamics (CFD). This involves importing a patient's CT scan into software (FLUENT 19.0, ANSYS Inc.) and inputting variables, such as air flow rate and temperature, so that the airflow field can be accurately simulated.[9] This allows the clinician to study how air flows within the channels (velocity, pressure, resistance) and not just the anatomy of the nose. These simulations have become more detailed, with increasing computer processing power, and open the possibility of patient-specific 'virtual surgery' whereby the impact of operative intervention using a virtual nose could be highly customized to the individual.[5,10-15]

Validation of CFD simulations has been previously attempted[16] using experimental measurements in a scaled-up rigid foam model of a 'healthy' nose (with no NAO).[17] The comparison validated the predictions of laminar-flow models applicable to restful breathing, but it also showed that more complex numerical models were needed to accurately predict the internal air flow at higher rates of breathing.

Objectives

The objective of this paper is to assess the predictions of the CFD model by comparing measurements of wall stress, pressure and nasal resistance in the virtual noses to its experimental counterpart using 3D printed rigid models under moderate breathing conditions. Modern CT scanning will be employed to produce high resolution virtual noses for the in-silico study, which are also converted into physical 3D-printed models, by additive manufacturing, for the experiments.

We also consider how an in-silico approach could be further developed, and employed, to improve surgical outcome for patients seeking septorhinoplasty.

Methods

Two subjects ('Subject A' and 'Subject B') were chosen from existing patient cone beam computed tomography (CBCT) scans, acquired as part of pre-operative work up. Subject A, with symptoms of nasal airway obstruction (NAO), was a 39 year old female with history of trauma to the nasal bridge resulting in a 'mid nasal third' deformity. The deformity involved the septum, upper lateral cartilages and tip of the nasal bone cap. This resulted in an external deviation and a compromised left nasal airway due to medial displacement of the upper lateral into the valve. Subject B, with no symptoms of NAO, was a 32 year old female requesting cosmetic rhinoplasty with an asymptomatic left maxillary

retention cyst. To benchmark the current findings, additional data from a 'Subject C' is included. It refers to published data obtained from a healthy 25 year old Asian male reported by Wen et al.[18]

Data from the CBCT was imported and reconstructed into a mesh for CFD models. 3D printed specimens were produced form the CBCT data. Experimental data were collected on airflow. The full experimental protocol and set up is described in the Supplementary Online-Only Material.[19]

All procedures performed in studies involving human participants were in accordance with the ethical standards of the institutional and/or national research committee and with the 1964 Helsinki Declaration and its later amendments or comparable ethical standards.

Results

Characterization of Nasal Airway Obstruction

The cross-sectional area (Figure 1), and subsequent velocity/pressure profiles, were compared along 14 coronal (X-Z) planes in the virtual nose (details in Supplementary Material[18]). Within the vicinity of the nasal valve, 1 – 3 cm from the nasal tip, the cross-sectional area is narrowest in all three subjects (<1 cm²). The right nasal channel of Subject A is 48-67% the area of the left side at this region (Figure 1b), corresponding to the static narrowing noted on the original CBCT scans at Y=2.4 cm (Supplementary Material Figure A1). The difference between left and right nasal channels (Figure 1b) was insignificant (<0.1 cm²) for all subjects beyond (Y>3 cm) the nasal valve.

Comparison of CFD predictions and Experimental Measurements

The predicted average wall pressure by CFD (defined as $\bar{P}_i = \int_{A_i} P_i dA_i / A_i$, where P_i is the pressure acting on an elemental area dA_i within the total area A_i of the pressure tap in the experimental prototype) was compared to its experimental counterpart in Figure 2. The static pressures measured experimentally were negative in all cases since suction was applied to the nasopharynx end of the models to simulate inspiration. At each of the three locations in each nasal channel of both subjects, the CFD predictions agreed with the experimental data.

The pressure profiles in each nasal channel of Subject B (Figure 2b) are comparable (left: -4.5 to -7.0 Pa, right: -5.2 to -8.5 Pa) and follow a similar trend to the pressure profile of the unobstructed left nasal channel (-4.5 to -5.5 Pa) of Subject A (Figure 2a). The right nasal channel of Subject A approximately doubles the wall pressure at all three points (-10.0 to -12.5 Pa) both in the virtual nose and experimentally.

Effects of NAO on Air Flow

To provide a qualitative visualisation of the flow field, streamlines (family of curves that are instantaneously tangent to the velocity vector of the air flow) in channels of both subjects are plotted in Figure 3. In the non-obstructed channels (Figure 3a, c and d), the air flow is redirected towards the narrowest section: the nasal valve region. It then turns posteriorly, nearly 90°, towards the nasopharynx. Higher flow velocities are visible in the vicinity of the nasal valve. Subsequently, the air flow separates into the inferior, middle and superior meatuses of the nasal channel, where there is a convergence of streamlines, leading to an increase of the local flow velocity, in the middle and inferior meatuses of the nasal channels. In the main airway section, the velocity of the laminar flow remains largely unchanged.

The effect of NAO on the air flow field is shown in the obstructed right channel in Subject A (Figure 3b). Two notable results are observed. First, the maximum air flow velocity in this channel (7.89 m/s) is higher than the contralateral side (5.92 m/s in Figure 3a) whereas in subject B the maximum air flow velocities are the same (5.51 m/s in Figure 3c and d). Second, in the right channel of Subject A, the bulk of the airflow is forced to remain in the inferior meatus and a prominent vortex developed in the superior meatus.

The distribution of the anteroposterior velocity (V_Y) contours normal to the three coronal (X-Z) planes Y = 2.0 cm, 2.6 cm and 6.2 cm from the nasal tip is shown in Figure 4, with data from Subject C included for comparison[18] (see Supplementary Material for further illustrations of planes). Anteriorly, most flow occurs superiorly (Figure 4a). Posterior to this, as the nasal channel widens, the main flow field expands inside the space available with the exception of the obstructed right channel of Subject A (Figure 4b): instead, a section with negligible air velocity is seen to develop in the superior and inferior meatus of this channel leading to a higher flow velocity (approximately 4.1 m/s) across 95% of the non-obstructed channel area. At the turbinate region (see Figure 4c), the bulk of the airflow occurs close to the septum wall for all three subjects. The overall drop in airflow velocity corresponds to the increase in cross sectional area in this turbinate region (Figure 1).

Wall Static Pressure, Shear Stress, and Nasal Resistance

Coronal planes[18] were used to investigate the variation of the average wall pressure, shear stress, and nasal resistance with anteroposterior distance (Y axis) for the subjects A and B (Figure 5). Further details are available in the Supplementary Material.

The wall static pressure is averaged across the boundary of each cross section, defined by $\bar{P} = \int_L PdL/L$, where *P* is the pressure in across a contour segment of length *dL,* and *L* is the perimeter of the contour. The wall static pressure in the nasal valve region of the right airway in Subject A achieves its maximum absolute value (≈-11 Pa), increasing posteriorly to -10 Pa, the boundary condition imposed at the nasopharynx (Figure 5a). By contrast, in Subject B, the wall pressure in the nasal valve region decreases to only 60% of its terminal value. There is a small difference in wall pressure profile noted between left and right channel in Subject B.

Incremental nasal resistance is defined by $R_i = \Delta P_i / \dot{Q_{ul}}$ where ΔP_i is the incremental pressure difference across two sequential cross-sections and $\dot{Q}_{ul}$ is the unilateral flow rate. Figure 5b demonstrates peak incremental nasal resistance in the obstructed right channel of Subject A (2.8 times the pressure in the contralateral channel and 5.8 times the incremental pressures noted in Subject B at 1.7 cm from the nasal tip).

Wall shear stress averaged over the boundary of each coronal (X-Z) plane section is calculated according to $\bar{\tau}_i = \int_{L_i} \tau_i dL_i / L_i$, where τ_i is the shear stress in across a contour segment of length dL_i, and L_i is the perimeter of the contour. Figure 5c shows the average wall shear stress of the obstructed right channel of Subject A is approximately double that of the rest.

Discussion

Comparison of the Virtual Nose with the 3-D printed nose

The static pressures obtained from experimental measurements on the 3D printed noses are in good agreement with those predicted by numerical simulation in the virtual noses (Figure 2). The CFD and experimental results were within experimental and variational discrepancies, introduced by the finite area of the pressure sensors, and the averaging of pressure in this area. In principle, any tube intrusion and the surface roughness of the 3D printed prototypes can affect flow features, however in this study this influence was found to be negligible.

Commentary on the Effects of NAO on Air Flow

The images of the flow fields (Figure 3) demonstrate that the majority of the air flow occurs in the inferior parts of the channels. This is likely because the inferiorly-directed nasopharynx posteriorly provides the negative driving pressure during inspiration.

The obstructed right channel of Subject A has a higher maximum velocity (7.89 m/s, Figure 3b) and there is a prominent vortex in the vicinity of the obstruction. This vortex is generated by the pressure

gradient caused by the abrupt increase in the cross-sectional area of the channel at the obstruction, and this highlights the importance of capturing this phenomenon accurately in the virtual nose. Posterior to the obstruction there is a 'zero-flow zone' caused by the anterior blockage, which accelerates the flow in the anterior region and reduces the time for airflow diffusion as the cross-sectional area increases. This is consistent with similar observations reported by others.[18,19]

The Virtual Nose as an objective assessment of a subjective symptom

The nasal valve is the flow limiting region of the nose[2], the narrowest part when air flows inward in a generally anteroposterior direction. This is true for both Subjects A and B and also the benchmark study Subject C[18] (Figure 1). An obstruction in this area increases significantly (2 - 4x) the wall pressure, shear stress, and nasal resistance, all of which have been shown in the literature to correlate with patient perception.[9]

Nasal resistance can contribute up to half the total airway resistance and previous work has used the pressure differential across the nostril and the nasopharynx as a whole.[9] In this paper, we have demonstrated the possibility of a greater degree of granularity (incremental nasal resistance) since CFD allows capture of detailed measurements from within the virtual noses.

Interestingly, the widening of the channel in Subject A posterior to the obstruction has little influence on the incremental nasal resistance and wall stress (Figure 5) which is far greater in the nasal valve region and may better explain the symptoms and, hence, perception of NAO.

The models in this paper are based on static CBCT scans. The discrepancy between the non-obstructed left and right channels of Subject B, which was in any case <0.1cm², may be attributed to natural anatomical variation or part of the circadian variation in physiological congestion[20]. Natural anatomical variation beyond the nasal valve may be imperceptible and negligible compared with the effects of the nasal valve which, by definition, is the rate limiting region of the nasal structure to airflow. Physiological variability in the left and right nasal channels is part of the nasal cycle whereby relative patency of the two nasal channels due to the levels of congestion varies as part of a circadian cycle.[20] This latter consideration is of course the caveat emptor for the surgeon interpreting any static CBCT scan.

Application of Virtual Noses to assess NAO in clinical practice

Detailed assessment of the NAO can be performed with CFD. Velocity flow fields and the location of vortices give a visualisation of the effect of the NAO as they form just posterior to the obstruction in Subject A (Figure 3). Velocity maps in the coronal (X-Z) plane allow a different perspective where the NAO is visualised by examining for low flow areas posterior to the obstruction (Figure 4). Average static pressures, incremental nasal resistances, and average wall shear stresses (Figure 5) might be used to quantify the degree of NAO and allow for objective assessment of outcomes of surgery, or for predictive outcomes.

Clearly, in order to be more accessible in the clinical setting, the technology needs to be usable by someone without the participation of software experts. Having demonstrated the usefulness of this method of assessment, this paper motivates further development of its automation so it may be more readily applied by the practising surgeon.[5] A CBCT scan could be automatically imported into software that generates graphics similar to those seen in Figures 1-5 enabling a surgeon to 'read' them like any other computerized scan and correlate these objective insights from within the virtual nose to the subjective descriptions of NAO given by the patient.

Future Study

The current simulations assume rigid nasal cavity wall, i.e. no change in cavity geometry during inspiration. A compliant cavity wall model would be particularly useful when considering revision rhinoplasty surgery in patients troubled by symptoms resulting from collapse of nasal structures during the negative pressures generated by inspiration, as seen in middle nasal valve collapse. A

moving virtual nose would be highly complex and contain many untested assumptions regarding the wall stiffness and change in shape.

Using the process described in this study, it is possible to validate simulations of dynamic virtual noses. e.g. incorporating fluid-structure interaction, using compliant 3D models printed as composites with varying Young's Moduli drawn from previously published data[21] in order to demonstrate differences in the resistance to airflow and change in shape during inspiration and hence airflow. This is part of an on-going investigation by the authors.

Conclusion

Although reconstruction of the patient nose in virtual reality requires assumptions about the physical properties of the nose and the air that travels within it, far more information about airflow (flow streamlines, velocity contours, pressure contours and wall shear stress) can be obtained from these virtual noses than using conventional techniques such as rhinomanometry and acoustic rhinometry *in vivo*.

CFD simulations on virtual noses both with and without symptoms of NAO agree with measured pressure and flow data from experiments using 3D–printed prototypes of these virtual noses from the same static CBCT scans. The new finding in this study is that the CFD calculations are validated with experimental measurements, and are valid for the mapping and detailed assessment of airflow characteristics affected by NAO. This proof of concept and the data generated by it may serve to be a key part of functional rhinoplasty surgery in the future.

References

1. Sundh C, Sunnergren O. Long-term symptom relief after septoplasty. Eur Arch Otorhinolaryngol 2015;272:2871-5.
2. Brandon BM, Austin GK, Fleischman G, et al. Comparison of Airflow Between Spreader Grafts and Butterfly Grafts Using Computational Flow Dynamics in a Cadaveric Model. JAMA Facial Plast Surg 2018;20:215-21.
3. Moreddu E, Meister L, Dabadie A, Triglia JM, Medale M, Nicollas R. Numerical simulation of nasal airflows and thermal air modification in newborns. Med Biol Eng Comput 2020;58:307-17.
4. Tripathi PB, Elghobashi S, Wong BJF. The Myth of the Internal Nasal Valve. JAMA Facial Plast Surg 2017;19:253-4.
5. Moghaddam MG, Garcia GJM, Frank-Ito DO, Kimbell JS, Rhee JS. Virtual septoplasty: a method to predict surgical outcomes for patients with nasal airway obstruction. Int J Comput Assist Radiol Surg 2020;15:725-35.
6. Doorly D, Taylor DJ, Franke P, Schroter RC. Experimental investigation of nasal airflow. Proc Inst Mech Eng H 2008;222:439-53.
7. Rennie CE. Investigation of Sinonasal Airflow and Transport [PhD Thesis]: Imperial College of Science, Technology and Medicine; 2013.
8. Kaneda S, Iida M, Yamamoto H, et al. Evaluation of Nasal Airflow and Resistance: Computational Modeling for Experimental Measurements. Tokai J Exp Clin Med 2019;44:59-67.
9. Radulesco T, Meister L, Bouchet G, et al. Functional relevance of computational fluid dynamics in the field of nasal obstruction: A literature review. Clin Otolaryngol 2019;44:801-9.
10. Garcia GJM, Rhee JS, Senior BA, Kimbell JS. Septal deviation and nasal resistance: An investigation using virtual surgery and computational fluid dynamics. Am J Rhinol Allergy 2010;24:46-53.
11. Guo YF, Shan YM, Cai HK, Chen XM, Gao XQ. [Simulation of inferior turbinate reduction using computational fluid dynamics methods]. Lin Chung Er Bi Yan Hou Tou Jing Wai Ke Za Zhi 2017;31:257-61.
12. Simmen D, Sommer F, Briner HR, et al. The effect of "Pyriform Turbinoplasty" on nasal airflow using a virtual model. Rhinology 2015;53:242-8.
13. Chen XB, Lee HP, Chong VF, Wang de Y. Impact of inferior turbinate hypertrophy on the aerodynamic pattern and physiological functions of the turbulent airflow - a CFD simulation model. Rhinology 2010;48:163-8.
14. Lee HP, Poh HJ, Chong FH, Wang de Y. Changes of airflow pattern in inferior turbinate hypertrophy: a computational fluid dynamics model. Am J Rhinol Allergy 2009;23:153-8.
15. Ozlugedik S, Nakiboglu G, Sert C, et al. Numerical study of the aerodynamic effects of septoplasty and partial lateral turbinectomy. Laryngoscope 2008;118:330-4.
16. Li C, Jiang J, Dong H, Zhao K. Computational modeling and validation of human nasal airflow under various breathing conditions. J Biomech 2017;64:59-68.
17. Hahn I, Scherer PW, Mozell MM. Velocity profiles measured for airflow through a large-scale model of the human nasal cavity. J Appl Physiol (1985) 1993;75:2273-87.
18. Wen J, Inthavong K, Tu J, Wang S. Numerical simulations for detailed airflow dynamics in a human nasal cavity. Respir Physiol Neurobiol 2008;161:125-35.
19. Wang de Y, Lee HP, Gordon BR. Impacts of fluid dynamics simulation in study of nasal airflow physiology and pathophysiology in realistic human three-dimensional nose models. Clin Exp Otorhinolaryngol 2012;5:181-7.
20. Kim HK, Kim HJ, Kim JH, Kim TH, Lee SH. Asymmetric expression level of clock genes in left vs. right nasal mucosa in humans with and without allergies and in rats: Circadian characteristics and possible contribution to nasal cycle. PLoS One 2018;13:e0194018.

21. Griffin MF, Premakumar Y, Seifalian AM, Szarko M, Butler PE. Biomechanical Characterisation of the Human Auricular Cartilages; Implications for Tissue Engineering. Ann Biomed Eng 2016;44:3460-7.

Supplementary Online-Only Material

Methods

CBCT data acquisition

CBCT data was collected using the 3D Accuitomo 170 Cone Beam Computed Tomography System (J. Morita Mfg. Corp, Kyoto, Japan) under the protocol of 90kV, 5mA, 17.5s exposure time, and 0.25mm voxel size (see Supplementary Material Figure A1).

Segmentation and mesh generation

CBCT scans were imported into the 3D medical imaging software Simpleware (Synopsys Inc., Mountain View, CA, United States) for volumetric reconstruction. The nasal channels were truncated anteriorly at the nostrils and posteriorly at the nasopharynx resulting in a 3D nasal cavity model. Paranasal sinuses and ethmoidal air cells were excluded from the reconstruction to reduce model complexity, similar to other studies[2]. Supplementary Material Figure A2 shows the volumetric reconstruction of the air channels within the nasal cavities of Subjects A and B.

The air channels were meshed using the mesh generation package Simpleware ScanIP. Majority of the volume mesh was generated using unstructured tetrahedral elements; in addition, seven layers of triangular prism elements were used to model the airway-cavity wall boundary layer (average thickness of 150 µm) to better capture the near-wall flow features. Supplementary Material Figure A3 shows a representative mesh of the airway channel, of a X-Z planar section located at Y = 4.5 cm from the nasal tip, for Subject B. A mesh-sensitivity study was performed and a converged model (using a criterion of $\leq$ 2.5 %) was achieved with approximately 3.3 million elements for both subjects.

CFD simulations

The models were exported in stereolithography file format and CFD simulations were performed using FLUENT 19.0 (ANSYS Inc., Canonsburg, PA, United States). Inlet and outlet boundary conditions were imposed at the nostril and X-Z plane just before the nasopharynx (Y = 8 cm in Supplementary Material Figure A3), respectively. A constant flow rate of 15 L/min was used for both subjects to simulate moderate breathing[16]; the experimental setup, to be described below, was used to obtain the flow rate in each channel, and the velocity inlet of each nasal channel was imposed according to $v_i = Q_i/A_i$, where Q_i and A_i are the flow rate and nostril area perpendicular to the inlet flow, respectively. These boundary conditions are tabulated in Supplementary Material Table 1. A pressure of -10 Pa was applied at the outlet boundary to replicate the negative static pressure in the nasopharynx[8,18]. The wall within the nasal cavity is treated as rigid, and a no-slip boundary condition is assumed at the air-cavity interface. Air is modelled here as a Newtonian fluid with properties identical to existing literature[2] as follows: constant density of ρ = 1.225 kg/m^3 and a viscosity of μ = 17.89 µPa at an ambient temperature of 15°C.

Nasal reconstruction by additive manufacturing (3D printing)

The 'positive' counterparts to Supplementary Material Figure A2 were generated using Simpleware ScanIP for 3D printing. A Boolean function was employed to subtract nasal cavity masks from the entire solid model. As a result, the 3D nasal models of both subjects have the shape of an 'external pyramid + a block', as illustrated in Supplementary Material Figure A4. Solid 3D models were manufactured using a stereolithographic 3D printer, with a transparent silicone resin that has a post-

cure tensile elastic modulus of 2.8 GPa. The elastic modulus is 9 orders of magnitude greater than the measured air pressure; hence, the nasal wall is assumed to be rigid.

Experimental setup

Three 4 mm diameter taps were drilled into the 3D printed specimens for static pressure tapping – their locations in Supplementary Material Figure A4 follow those reported in Wang et al.[19] A schematic of the experimental setup is shown in Supplementary Material Figure A5. A vacuum pump (Rotary Vane Pump VTE8, Rietschle Thomas) was connected to the outlet airway sections (choanae) of the 3D printed specimen via a Y-shape tube joint and rigid connector. The flow rate, controlled manually by a flow control valve, was measured by flowmeters (SMC PFMB7, RS Components) placed upstream of the Y-junction. Flexible transparent tubings were inserted into the six pressure tapping points, with the other ends attached to pressure sensors (Sensirion SDP816-125Pa, RS Components). Sensor readings were converted into analogue signals and transmitted to a myRIO I/O device (myRIO-1900, National Instruments). The signals were processed and recorded by LabVIEW 2019 (National Instruments, Austin, Texas, United States).

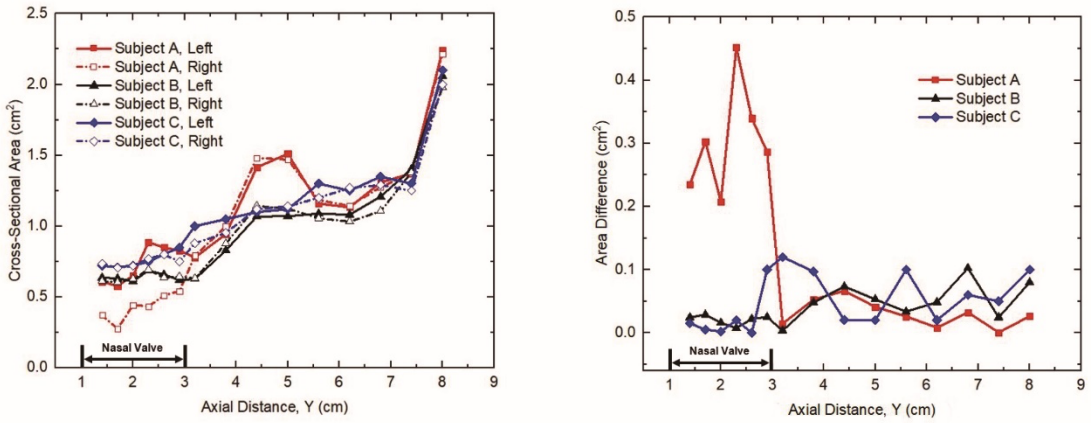

Figure 1

Variations in the nasal cross sectional area with anteroposterior axis (a); and, area difference between the left and right channel for each subject (b).

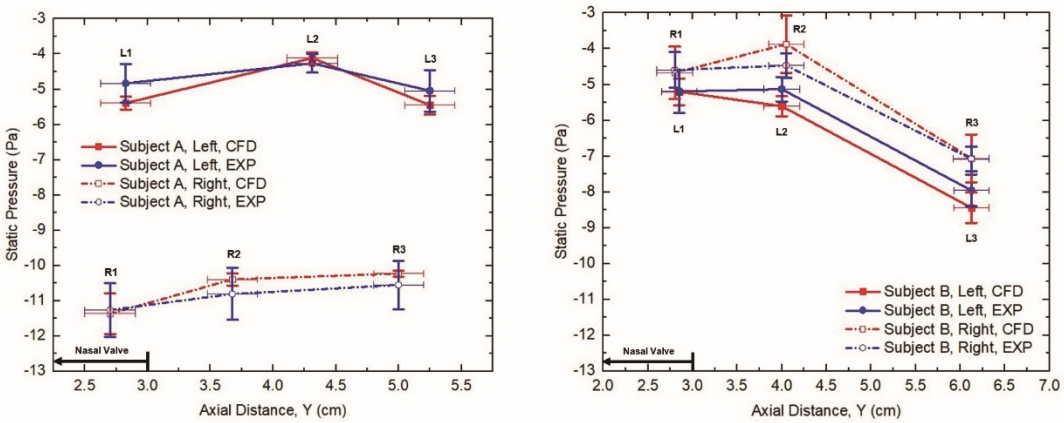

Figure 2

Comparison of static wall pressure in the experimental 3D printed and CFD virtual models. Vertical and horizontal error bars in the experimental data represent the measurement variance among the ≈5000 repeated measurements and diameter of the tapped hole, respectively. Vertical and horizontal error bars in the CFD data points represent the max/min variance of the local (element) pressure in the averaged area and diameter of the corresponding "tapped" area, respectively.

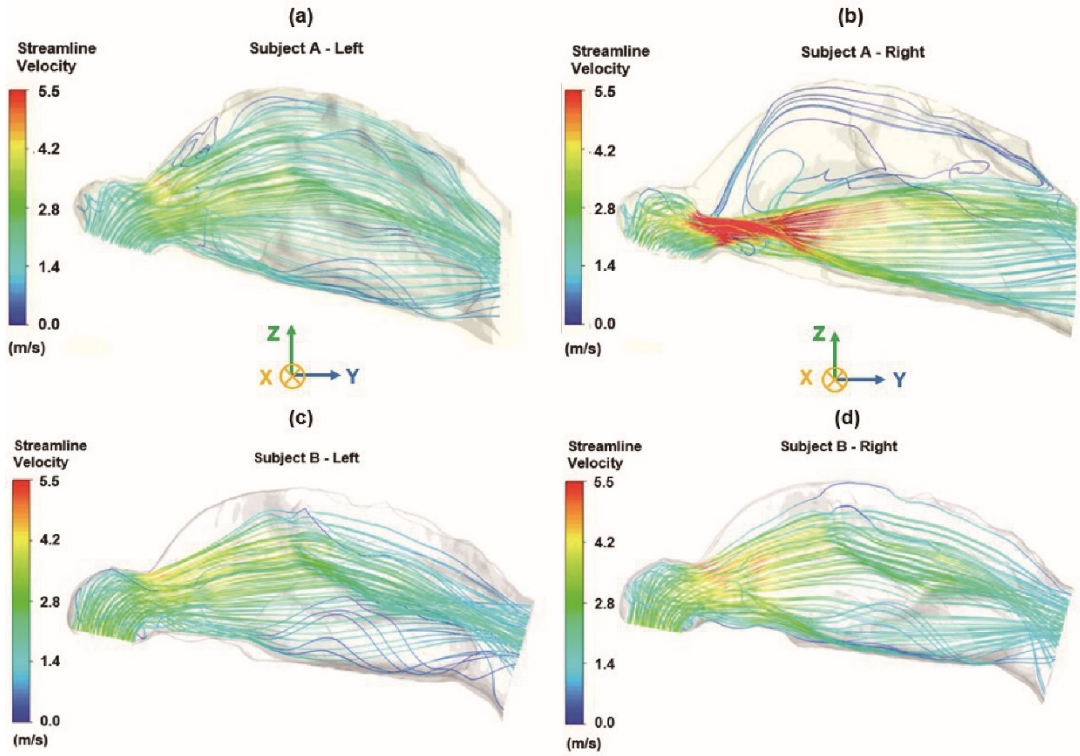

Figure 3

Streamlines of the flow in the nasal channels of Subject A (a and b), and Subject B (c and d).

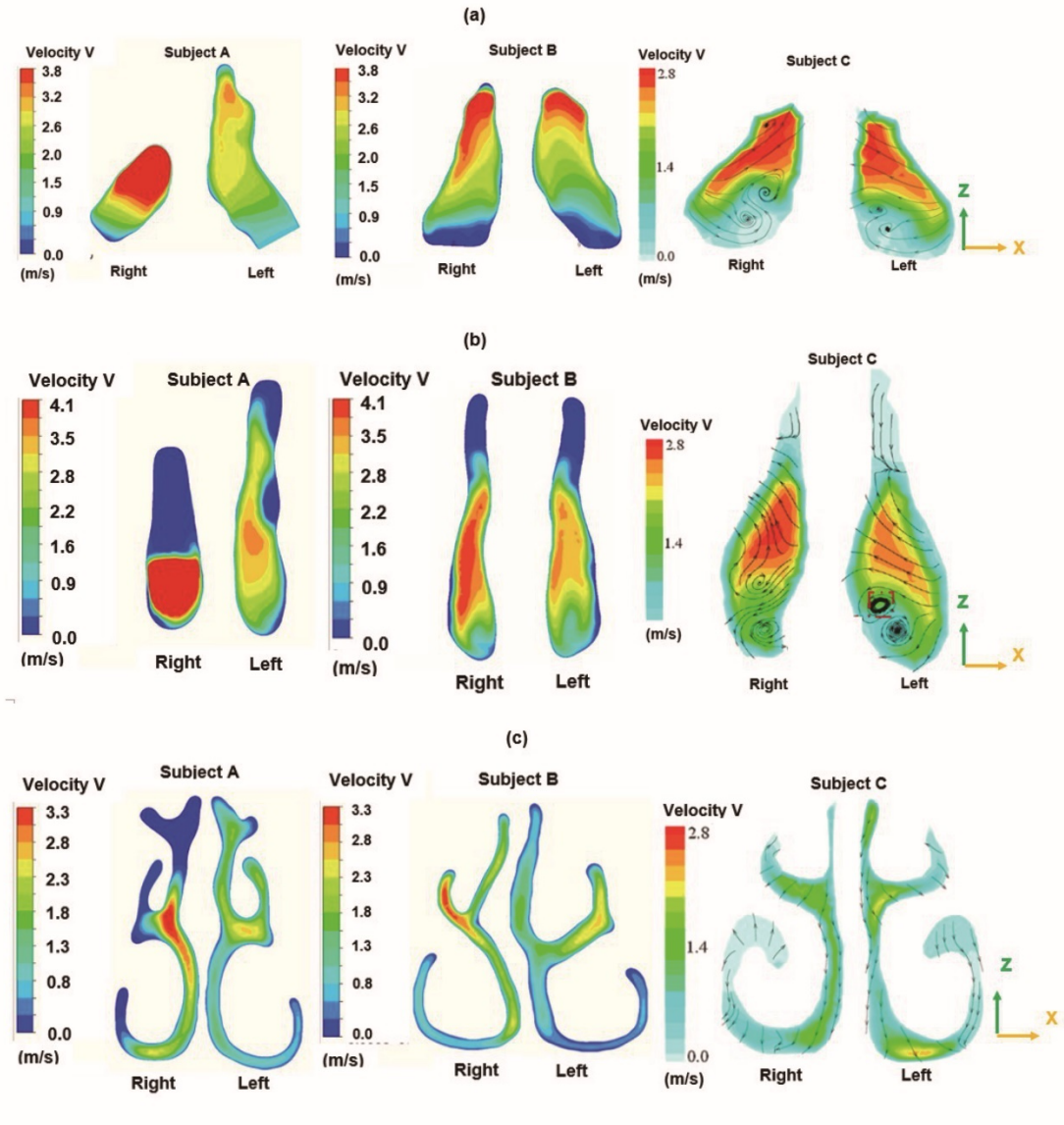

Figure 4

Distribution of normal velocity (v_Y) in planes 1-3 (a-c respectively) of Figure 5, for Subjects A, B, C. Subject C are taken from Wen et al[18]. All cross-sections shown are in a frontal perspective where positive flow is into the paper.

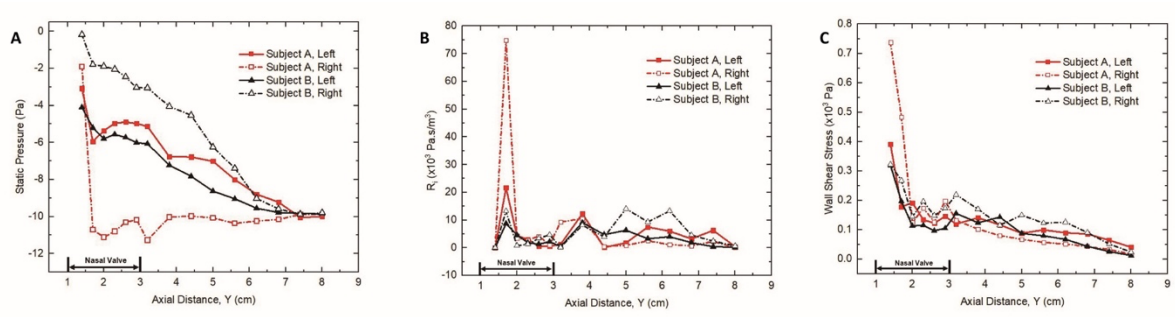

Figure 5

Variation of (a) static wall pressure, (b) incremental nasal resistance R_i and (c) wall shear stress, with the anteroposterior distance.

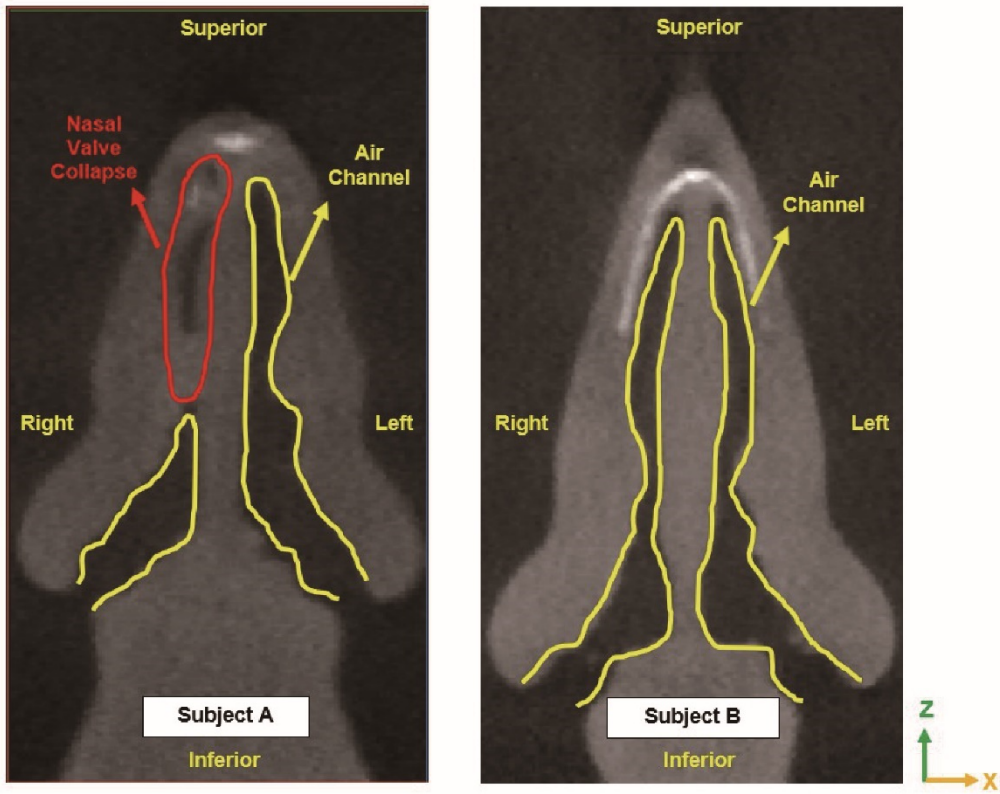

Figure A1 (Supplementary Online-Only Material)

Cone Beam Computerised Tomography (CBCT) scans of subject A (a), and B (b), showing coronal (X-Z) planes located at Y = 2.4 cm from the nasal tip. Approximate boundaries of the nasal air channels are highlighted in yellow, showing nasal airway obstruction (NAO) in the left channel of subject A.

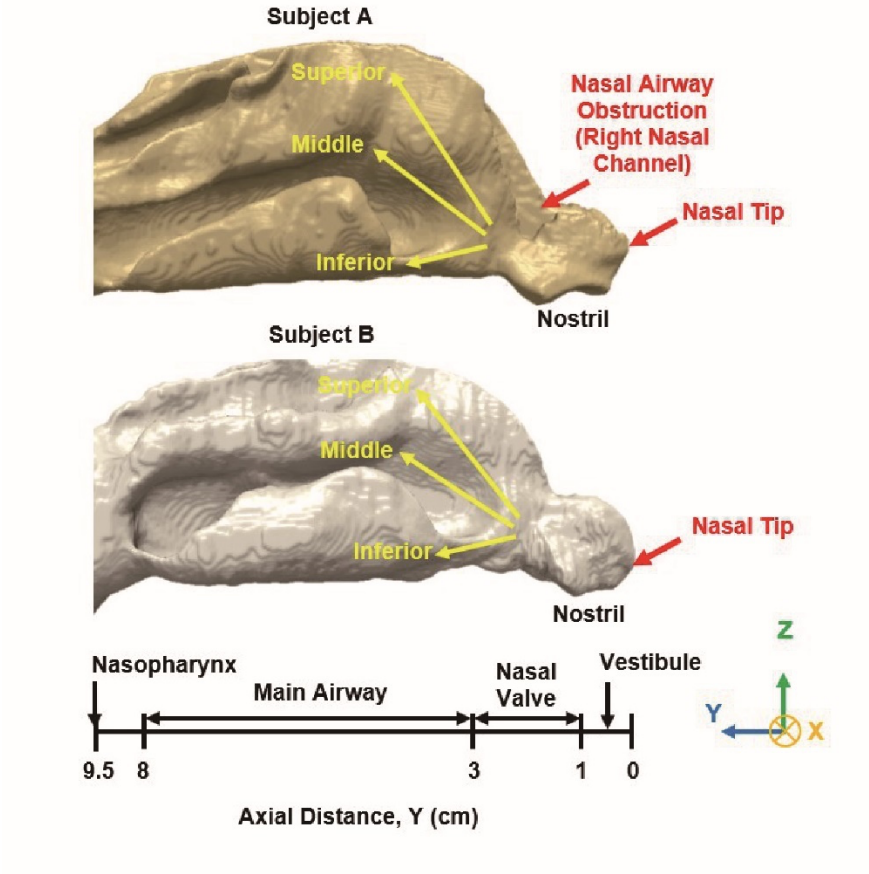

Figure A2 (Supplementary Online-Only Material)

Volumetric reconstruction of the nasal cavity in Subjects A and B, showing the inferior, middle and superior meatuses within the air channel. Location of nasal airway obstruction in Subject A, and the anteroposterior distance Y (Y=0 corresponds to the tip of the nostril) are as indicated.

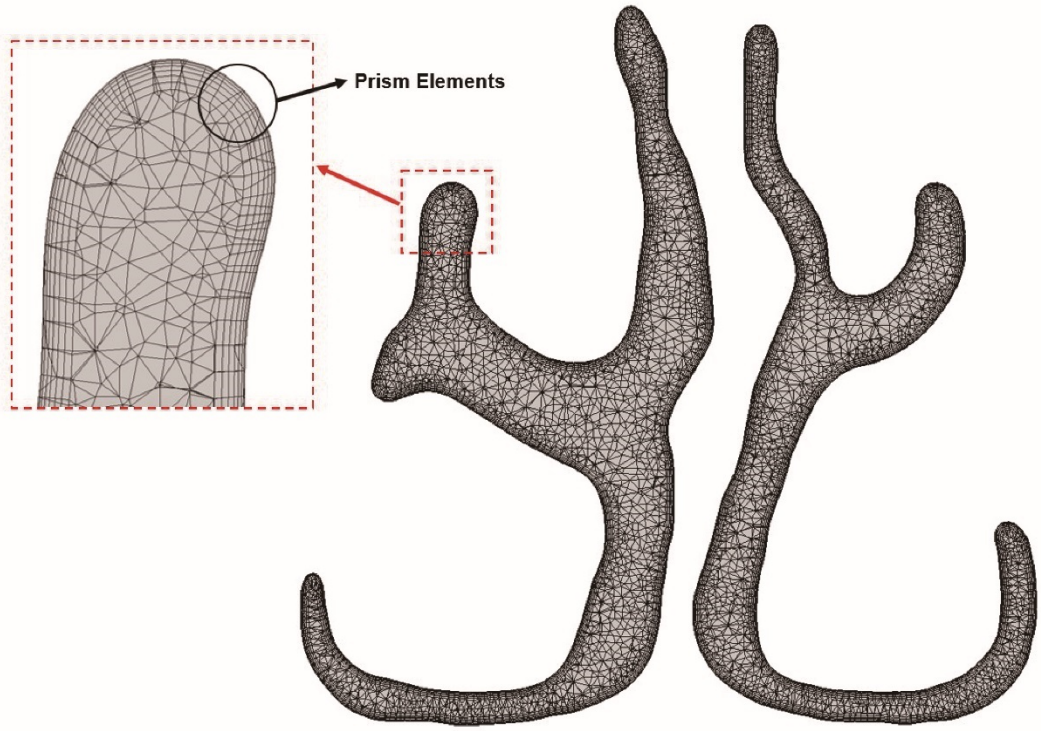

Figure A3 (Supplementary Online-Only Material)

Representative mesh of an airway channel, sectioned on a X-Z plane located at Y= 4.5 cm from the nasal tip, for Subject B.

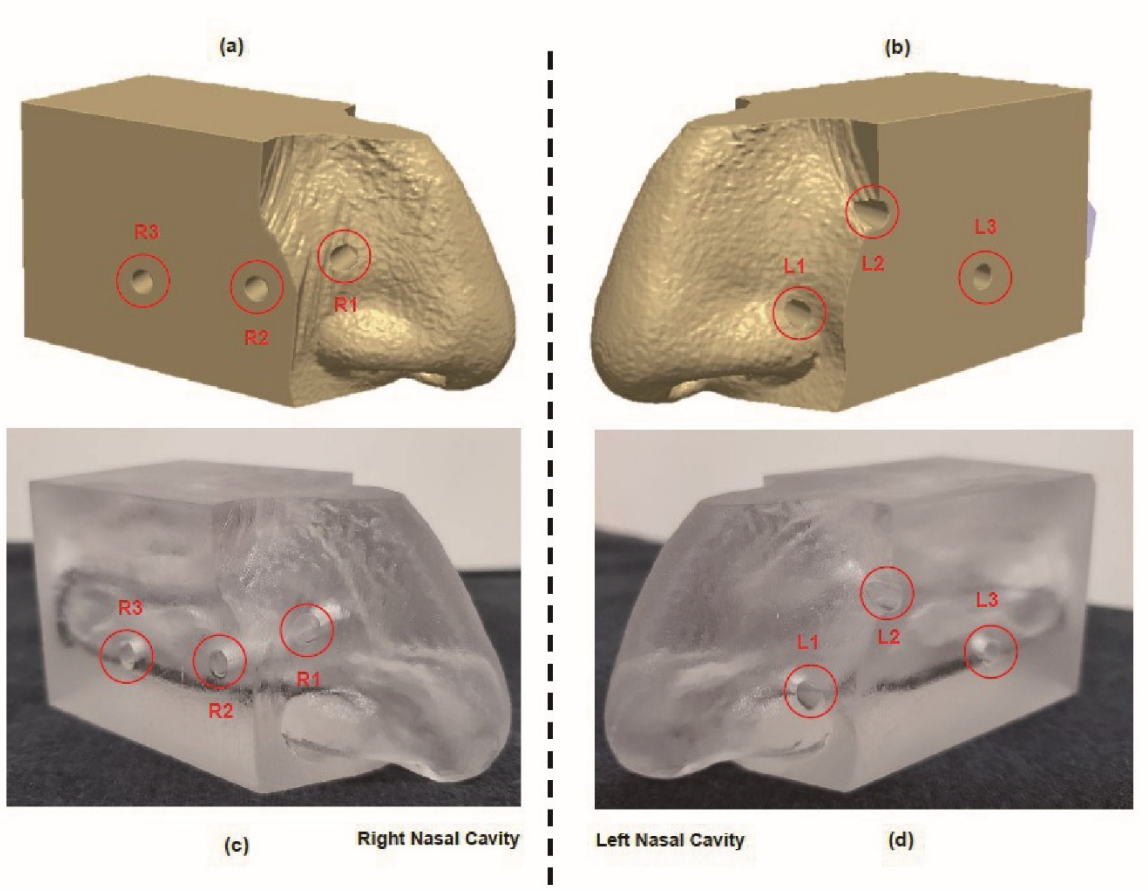

Figure A4 (Supplementary Online-Only Material)

Virtual (a and b) and 3D printed (c and d) reconstructions of the nasal structure for Subject A. Locations of the static pressure taps in the right (R1-R3) and left (L1-L3) air channels are circled.

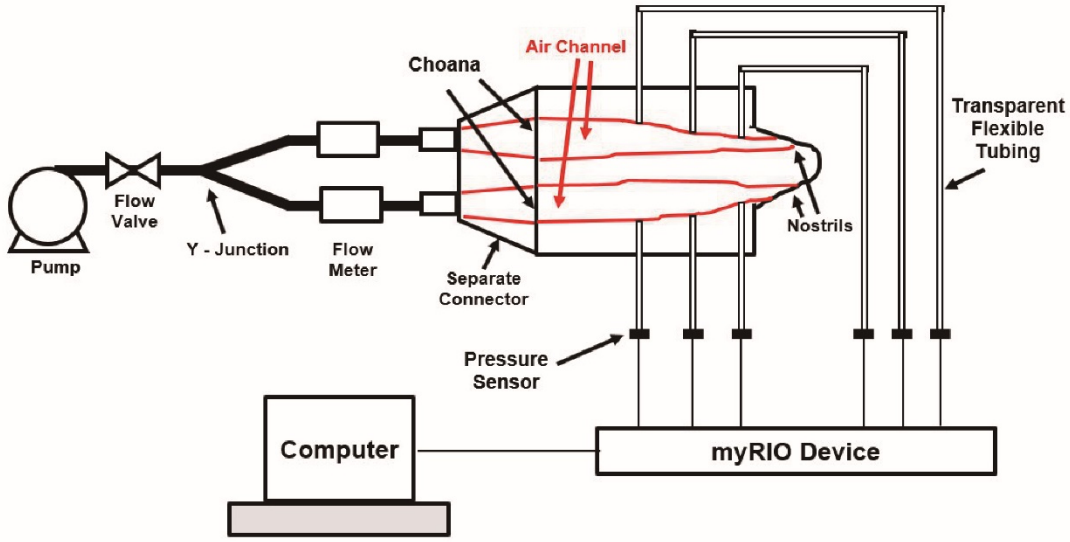

Figure A5 (Supplementary Online-Only Material)

Schematic of experimental set up.

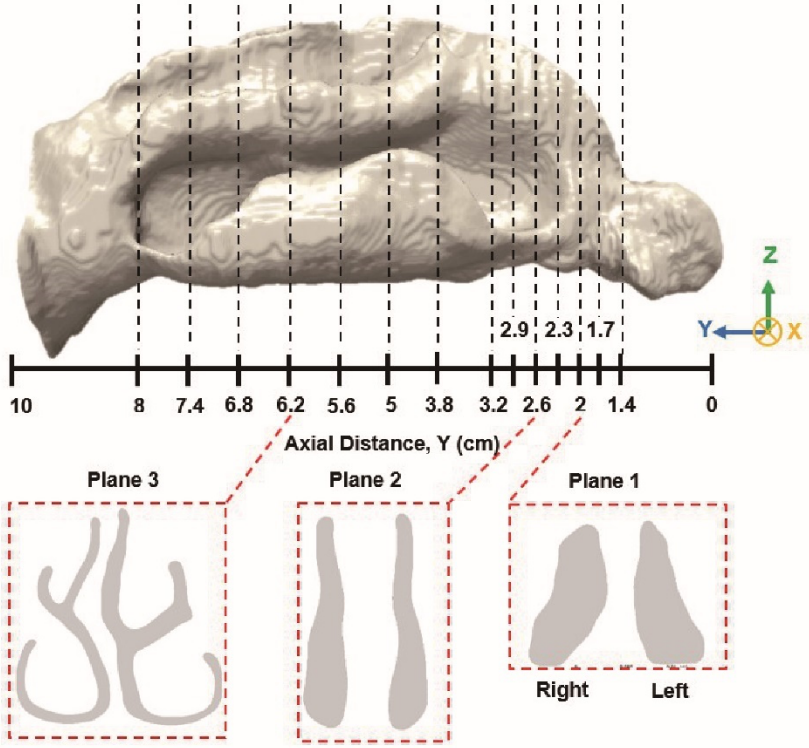

Figure A6 (Supplementary Online-Only Material)

Nasal channel profile along three representative coronal (X-Z) planes at Y = 2.0, 2.6, and 6.1 cm for subject B.